

Accepted Manuscript

Graphene on nickel (100) micrograins: Modulating the interface interaction by extended moiré superstructures

Zhiyu Zou, Virginia Carnevali, Matteo Jugovac, Laerte L. Patera, Alessandro Sala, Mirco Panighel, Cinzia Cepek, German Soldano, Marcelo M. Mariscal, Maria Peressi, Giovanni Comelli, Cristina Africh

PII: S0008-6223(18)30010-1

DOI: [10.1016/j.carbon.2018.01.010](https://doi.org/10.1016/j.carbon.2018.01.010)

Reference: CARBON 12751

To appear in: *Carbon*

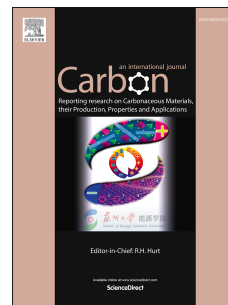
Received Date: 12 September 2017

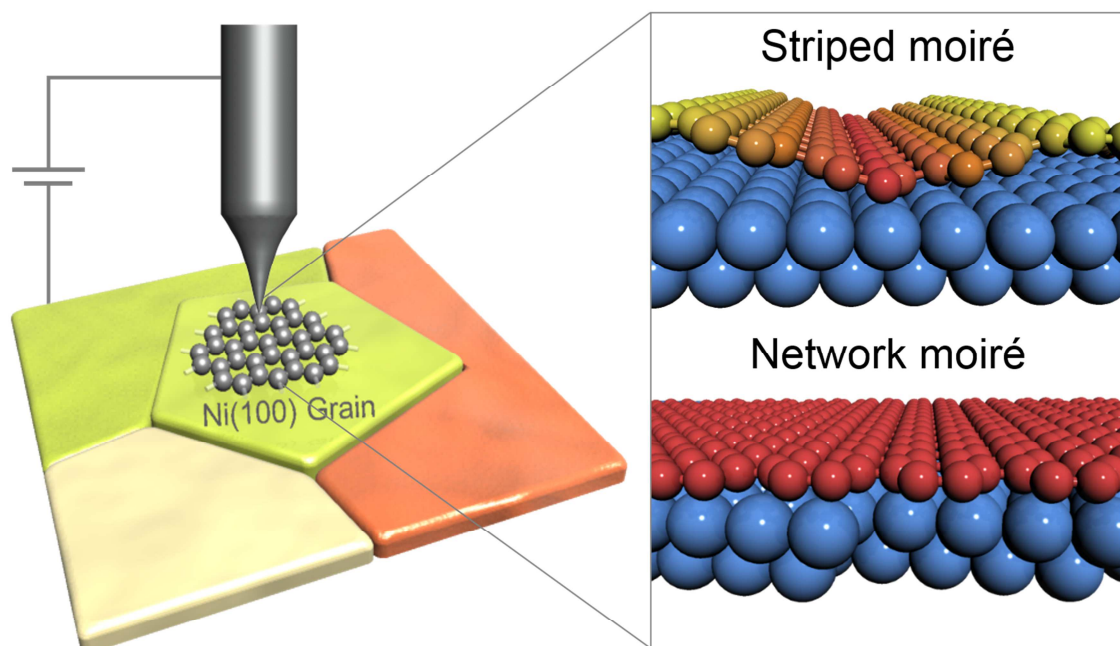
Revised Date: 22 December 2017

Accepted Date: 2 January 2018

Please cite this article as: Z. Zou, V. Carnevali, M. Jugovac, L.L. Patera, A. Sala, M. Panighel, C. Cepek, G. Soldano, M.M. Mariscal, M. Peressi, G. Comelli, C. Africh, Graphene on nickel (100) micrograins: Modulating the interface interaction by extended moiré superstructures, *Carbon* (2018), doi: 10.1016/j.carbon.2018.01.010.

This is a PDF file of an unedited manuscript that has been accepted for publication. As a service to our customers we are providing this early version of the manuscript. The manuscript will undergo copyediting, typesetting, and review of the resulting proof before it is published in its final form. Please note that during the production process errors may be discovered which could affect the content, and all legal disclaimers that apply to the journal pertain.





ACCEPTED MANUSCRIPT

Graphene on nickel (100) micrograins: modulating the interface interaction by extended moiré superstructures

Zhiyu Zou^{1,2,†}, Virginia Carnevali^{3,4}, Matteo Jugovac^{3,‡}, Laerte L. Patera^{1,3,§}, Alessandro Sala^{1,3}, Mirco Panighel¹, Cinzia Cepek¹, German Soldano⁵, Marcelo M. Mariscal⁵, Maria Peressi^{3,4,*}, Giovanni Comelli^{1,3}, Cristina Africh^{1,*}

¹CNR-IOM Laboratorio TASC, S.S. 14 km 163.5 - Basovizza, 34149 Trieste, Italy.

²Abdus Salam International Centre for Theoretical Physics, Strada Costiera 11, 34151 Trieste, Italy

³Department of Physics, University of Trieste, via A. Valerio 2, 34127 Trieste, Italy

⁴CNR-IOM DEMOCRITOS National Simulation Center, via Bonomea 265, I-34136 Trieste, Italy

⁵INFIQC, CONICET and Departamento de Química Teórica y Computacional, Facultad de Ciencias Químicas,

Universidad Nacional de Córdoba, Haya de la Torre, 5000 Córdoba, Argentina

*Corresponding authors. Tel: +39 0403756443 (Cristina Africh); +39 0402240242 (Maria Peressi). E-mail: africh@iom.cnr.it (Cristina Africh); peressi@ts.infn.it (Maria Peressi)

[†] Present address: Institute of Applied Physics, Vienna University of Technology, 1040 Vienna, Austria

[‡] Present address: Peter Grünberg Institute (PGI-6), Research Center Jülich, 52425 Jülich, Germany

[§] Present address: Institute of Experimental and Applied Physics, University of Regensburg, D-93053 Regensburg, Germany.

ABSTRACT

Interaction with the substrate strongly affects the electronic/chemical properties of supported graphene. So far, graphene deposited by chemical vapor deposition (CVD) on catalytic single crystal transition metal surfaces - mostly 3-fold close-packed - has mainly been studied. Herein, we investigated CVD graphene on a polycrystalline nickel (Ni) substrate, focusing in particular on (100) micrograins and comparing the observed behavior with that on single crystal Ni(100) substrate. The symmetry-mismatch leads to moiré superstructures with stripe-like or rhombic-network morphology, which were characterized by atomically-resolved scanning tunneling microscopy (STM). Density functional theory (DFT) simulations shed light on spatial corrugation and interfacial interactions: depending on the misorientation angle, graphene is either alternately physisorbed or chemisorbed or uniformly chemisorbed, the interaction being modulated by the (sub)nanometer-sized moiré superstructures. Ni(100) micrograins appear to be a promising substrate to finely tailor the electronic properties of graphene at the nanoscale, with relevant perspective applications in electronics and catalysis.

1. Introduction

Research in graphene adsorption on transition metals has witnessed an unprecedented prosperity for the last decade, owing to the rich electronic and chemical properties induced at the interfaces[1-2], and also benefitting from the rapid development of the chemical vapor deposition (CVD) method for graphene production[3-8]. In fundamental studies, the close-packed (111)/(0001) faces of fcc/hcp transition metals are generally utilized as catalytic substrates for graphene epitaxial growth, due to their high thermodynamic stability and compatible symmetry with graphene. In particular, on nickel (Ni) (111) and cobalt (Co) (0001) at specific growth conditions graphene can take the (1×1) registry with respect to the substrates, due to the very small lattice mismatch (2.46 \AA for graphene vs. $2.49/2.50 \text{ \AA}$ for Ni(111)/Co(0001)), as well as to the relatively strong interfacial coupling (i.e. chemisorption)[9-12]. For other strongly interacting systems, e.g. graphene on ruthenium (Ru) (0001), rhodium (111), rhenium (0001), etc., the large lattice mismatch cannot be accommodated by the elongation of the C-C bonds. As a consequence, moiré superstructures generally composed of a single rotational domain are found; the accumulated strain is released by a significant buckling of the graphene lattice, which leads to alternate strongly- and weakly-interacting regions across the moiré supercells[13-18]. In contrast, the weak coupling between graphene and other transition metals (such as copper (Cu), iridium (Ir) and platinum) results in large interfacial spacing out of the range of chemisorption, smaller spatial corrugation of moirés with respect to strongly-coupled systems, and limited rotational alignment between graphene and the substrate[19-23]. From an electronic point of view, the band structures for chemisorbed graphene (such as that on Ni(111) or Ru(0001)) are fragmented or disrupted due to the hybridization of the graphene π state and the metal d orbital, while physisorbed graphene typically shows Dirac cones similar to its pristine form[24-26]. Therefore, the magnitude of energy gap opening, interface charge

redistribution and π band shift from the Fermi level can all be used as fingerprints of the interaction intensity between overlayer and substrate.

The well-established knowledge on the interaction between graphene and three-fold single crystal surfaces, however, is inadequate to rationalize the behavior on realistic substrates used for graphene growth and applications, where polycrystalline transition metal substrates are typically utilized. This is because polycrystalline metals used for graphene growth are generally composed of grains exposing a variety of surface orientations, e.g. (111), (100), and (110) orientations in fcc transition metals[27-29]. It is therefore highly important to understand the interaction between graphene and metal surface with an interfacial symmetry mismatch. As reported on Cu(100), Ir(100), iron (110) and Ni(110), graphene moirés induced by the lattice mismatch with the substrate can present striped- or, sometimes, rhombic-network morphology, characterized by varying interaction strength with the substrate[30-35]. However, the field related to the symmetry-mismatched graphene-metal interfaces is still only partially explored and sometimes of controversy[35-36], therefore leaving plenty of room for further research.

In this context, we report on a systematic study of graphene adsorption on the (100) surface of nickel, by means of high-resolution scanning tunneling microscopy (STM). Besides single crystals, (100) micrograins from polycrystalline Ni foils are also explored, thereby bridging the material gap from single crystal to realistic, non-ideal surfaces for STM measurements. Indeed, the (100) facet is one of the most common orientations present in polycrystalline Ni foils or thin films, as reported in literature[29, 37] and further corroborated in this work. In addition, nickel is among the class of most-utilized metallic catalysts for CVD growth of graphene[5-6, 38]. This work is therefore of potential interest for the scalable production and applications of graphene. Our results indicate that graphene structures observed on both single- and poly-crystalline substrates are highly

comparable, which guarantees the reliability of knowledge transfer from single crystalline surfaces onto the counterparts in polycrystalline metals. Due to the different symmetries between overlayer and substrate, a distribution of graphene rotation angles has been discovered, which leads to variant moiré superstructures. The moiré superstructures transform from stripe-like to rhombic modulations with the increase of angular misorientation, which unifies the previous observations on other 2- and 4-fold surfaces[30]. Parallel DFT simulations demonstrate that the transformation of moirés is accompanied by a variation of graphene adsorption behavior, from coexistence of alternating physis- and chemisorbed regions to exclusive chemisorption, indicating the potential to tailor the electronic or chemical properties of graphene at the nanometer scale.

2. Methods

2.1 Experimental methods

2.1.1 *Pretreatment of polycrystalline Ni foils.* The polycrystalline Ni foils were purchased from Sigma-Aldrich (thickness: 0.125 mm, purity: > 99.9%). The surface was flattened by mechanical polishing, followed by ultrasonic cleaning in DI water, ethanol and acetone. A 12-hour annealing at 900 °C in hydrogen and nitrogen at atmospheric pressure was applied to further improve the crystallinity of the Ni foil and remove the trace contaminant and residual carbon in the bulk. Before STM measurements, the sample was treated in a homemade ultrahigh vacuum (UHV) chamber with several sputtering and annealing cycles until X-ray photoemission spectroscopy (XPS) showed no contaminant elements left on surface (except trace carbon) at room temperature or graphene growth temperatures (400-600 °C).

2.1.2 *STM measurements.* STM experiments were carried out in a UHV chamber (base pressure: 1×10^{-10} mbar) equipped with standard sample preparation/characterization facilities and an Omicron variable temperature STM (VT-STM). Both Ni(100) single crystal and pretreated polycrystalline Ni foil were cleaned via several argon ion

sputtering and annealing (600 °C) cycles. The cleanness and crystallinity of the single crystal surface were checked by low energy electron diffraction (LEED).

Graphene was grown by either interstitial carbon segregation or ethylene exposure ($p = 5 \times 10^{-8} - 5 \times 10^{-6}$ mbar) at 400-600 °C. STM images were all acquired at room temperature except figure 2(a), which was taken at 450 °C. All the STM images were processed by Gwyddion[39]. LEED images were all taken with electron beam energy of 70 eV.

2.2 Theoretical methods

2.2.1 DFT calculations. DFT calculations were performed with Quantum ESPRESSO code[40], using plane-wave basis set and the Generalized Gradient Approximation for the exchange-correlation functional in the Perdew-Burke-Ernzerhof parametrization (GGA-PBE)[41]. In order to describe the graphene/Ni(100) interaction correctly, semi-empirical corrections accounting for the van der Waals interactions were included with the DFT-D approach[42]. Convergence tests suggested a kinetic energy cutoff of 30 Ry for the plane-wave basis set. The equilibrium lattice parameters characterizing the clean Ni(100) surface and the free-standing graphene are 2.49 Å and 2.46 Å respectively, equal to the experimental values. A periodically repeated slab geometry with 3 Ni layers and graphene adsorbed on one side was used, with a vacuum spacing of 13 Å between graphene and the parallel consecutive Ni(100) surface. In plane, the dimensions of the simulation cells are different according to the misorientation angle. With respect to the Ni(100) surface lattice, the simulation cells used throughout the work for s-moiré and n-moiré are a rectangular (12×1) supercell and a square ($\sqrt{13} \times \sqrt{13} R_{33.7^\circ}$) supercell, respectively (figure 3). Tests with different cell sizes have been performed (see figure S11). Concerning the Brillouin zone sampling, we adopted Monkhorst-Pack k-point meshes[43] and the Methfessel-Paxton smearing technique with an energy broadening of 0.01 Ry[44]. For s-moiré and n-moiré, 1×12×1 and 4×4×1 k-point grids centered on the Gamma point were used, respectively. The optimized atomic positions have been obtained minimizing the forces acting on each atom. The adsorption energy of graphene over Ni(100) was computed as $E_{ads} = E_{G/(100)} - E_G - E_{(100)}$, where $E_{G/(100)}$ is the total energy of the system, while E_G and $E_{(100)}$ are the energies of graphene and Ni(100) slab separately. In this calculation, the structure of graphene was considered frozen with the corrugation corresponding to the specific misorientation angle. Stick-and-ball models were rendered with the VMD software[45].

2.2.2 *STM simulations.* STM simulations were performed using the Tersoff-Hamann approach[46], according to which the tunneling current is proportional to the Integrated Local Density of States (ILDOS). The energy integration is performed in an energy window corresponding to the bias voltage used in the experiments. To simulate the constant current mode, we map the profile of an ILDOS isosurface laying within a certain height range over the graphene.

3. Results and discussion

3.1 STM measurement of graphene covered single-crystalline and polycrystalline, micro-grained Ni(100)

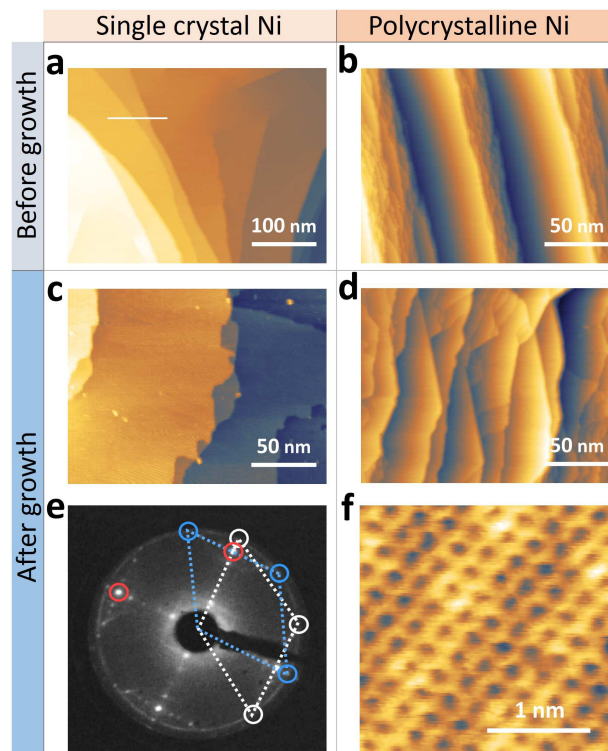


Figure 1 (a,b) Large-scale STM images acquired on the clean surfaces of (a) Ni(100) single crystal [$V_b = -0.3$ V, $I_t = 0.5$ nA] and (b) (100) oriented grain of polycrystalline Ni foil [$V_b = 0.2$ V, $I_t = 0.1$ nA]. (c,d) Large-scale STM images of graphene-covered surfaces (see Methods for experimental details). (c) Ni(100) single crystal [$V_b = 1.0$ V, $I_t = 0.2$ nA]. (d) (100) oriented grain of polycrystalline Ni foil [$V_b = 0.6$ V, $I_t = 0.3$ nA]. Considering the large

height variation on different terraces in (b,d), the average plane is artificially tilted to visualize the details of the whole image. (e) LEED pattern (70 eV) with graphene diffraction spots (surrounded by white and blue circles). The unit cells of two rotationally equivalent reciprocal graphene lattices are denoted as white and blue rhombuses. (f) Atomically resolved image of graphene taken on a flat terrace [$V_b = 0.15$ V, $I_t = 20$ nA].

Figure 1(a) presents a typical image of a single-crystal Ni(100) surface, exhibiting atomically flat terraces up to 100 nm wide, atomic steps and screw dislocations. The two consecutive steps along the white line exhibit height differences of 1.74 and 3.46 Å (one and two atomic layers, respectively, figures S1 and S2).

Moving to a polycrystalline sample, where high-resolution STM imaging is usually much more challenging than on single crystals[9], multistep pretreatments were adopted to improve the surface flatness and crystallinity (see Methods and figure S3). The existence of (100) oriented grains is evidenced in the X-ray diffractogram (XRD) of the sample (figure S4), with a peak intensity comparable to that of the most thermodynamically stable (111) facet, indicative of a considerable weight of this termination on the polycrystalline surface, in accordance with previous works[29, 37]. As a consequence, the (100) termination substantially contributes to graphene CVD growth on polycrystalline nickel substrates, making the investigation of graphene on this termination relevant also to scalable CVD production. We acquired STM images on different regions of the pretreated polycrystalline Ni foil, revealing the co-existence of quite rough and flat grains, most of the latter exhibiting (100) facets. Although still more corrugated than in single crystals, the surface morphology of the selected (100) grain, characterized by flat terraces as wide as tens of nanometers separated by jagged step bunches (figure 1(b)), allowed for atomically resolved STM imaging, providing the grain orientation (figures S5 and S6).

Graphene was prepared on both single- and poly-crystalline nickel in the 400-600 °C temperature range, as previously reported for Ni(111) (see also Methods)[47]. As shown in figures 1(c,d), graphene growth dramatically changes the overall surface morphology: on both surfaces, the ragged step edges transform into smoother and locally linear frontiers. Atomic-resolved STM images clearly show the presence of the honeycomb network on both single (not shown) and polycrystalline (figure 1(f)) samples, thus confirming the successful production of a highly-crystalline graphene layer. Notably, the high resolution obtained on the polycrystalline foil clearly confirms also for nickel the feasibility of STM measurements on non-ideal, highly stepped surfaces with appropriate pre-processing, as previously reported for copper[27].

Figure 1(e) exhibits the LEED pattern of Ni(100) single crystal after growth of graphene at 600 °C. An almost continuous bright ring just outside the first-order diffraction spots of Ni(100) surface (marked in red) corresponds to several rotated graphene domains, indicative of a mosaic, polycrystalline nature of graphene at the mesoscale. However, the LEED pattern reveals two predominant orientations of graphene, evidenced by two six-fold sets of diffraction spots highlighted with white and blue circles and characterized by rhombic unit cells. Considering the 6-fold symmetry of graphene and the 4-fold symmetry of Ni(100) (figure S7), these two predominant orientations are equivalent and rotated by 30° from each other, with one graphene lattice vector oriented along either the [011] or [01 $\bar{1}$] direction of the substrate. Furthermore, the LEED spots along the main substrate directions suggest that these structures are commensurate, with (12 × 1) periodicity. To quantify the orientation of graphene with respect to the Ni(100) surface, herein we define the misorientation angle ϑ as the smallest angle between one zigzag direction of graphene and the lattice vectors of Ni(100) surface (see SI and figure S7). Thus, the two predominant graphene domains have both $\vartheta = 0^\circ$. The separate arcs in LEED are

symmetric around $\vartheta = \pm 15^\circ$, which is the largest possible angular misorientation between graphene and Ni(100) (figures S8, S9).

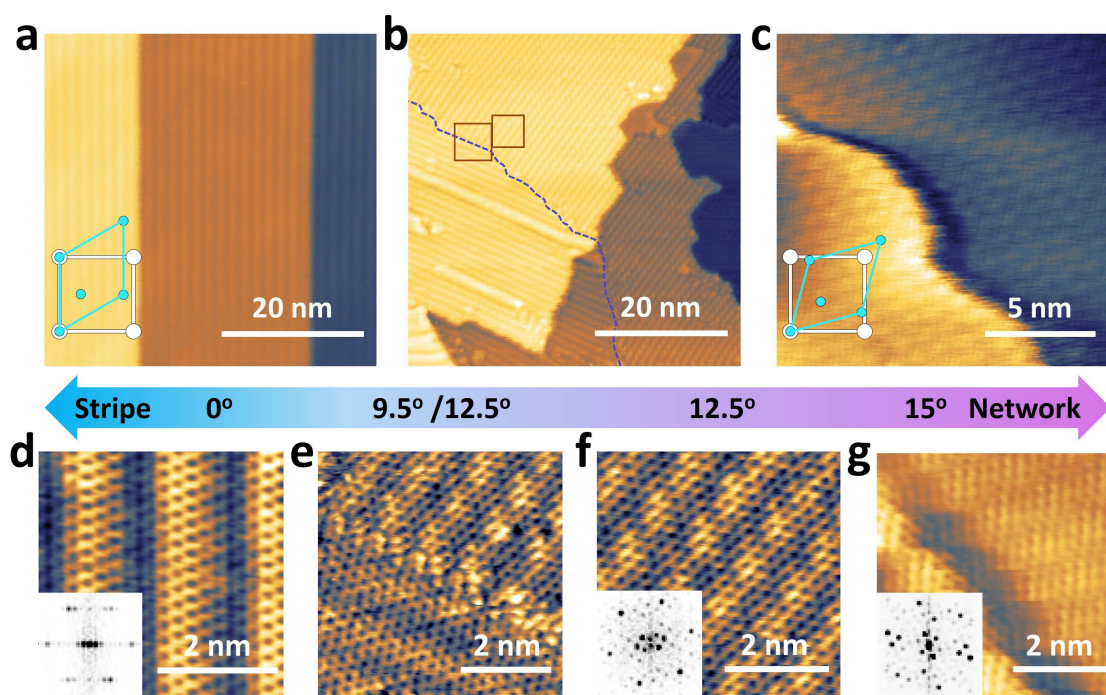


Figure 2 (a-c) STM topographic images of representative graphene moiré patterns exhibiting different periodicity and morphology (stripe & rhombic network). The graphene misorientation angles (ϑ) are: (a) $\sim 0^\circ$ [$V_b = 0.3$ V, $I_t = 0.3$ nA]; (b) left: 9.5° , right: 12.5° (separated by the domain boundary as a blue dashed line) [$V_b = -0.3$ V, $I_t = 0.3$ nA]; (c) 15° [$V_b = 0.005$ V, $I_t = 5$ nA]. The double-headed arrow indicates the range of possible misorientation angles. (d-f) Atomically resolved structures of the moirés shown in (a-c). (d) $\vartheta = 0^\circ$ [$V_b = 0.02$ V, $I_t = 5$ nA]. (e) Zoom-in at the left square in (b). $\vartheta = 9.5^\circ/12.5^\circ$ in the lower/upper part [$V_b = 0.15$ V, $I_t = 20$ nA]. (f) Zoom-in at the right square in (b). $\vartheta = 12.5^\circ$ [$V_b = 0.15$ V, $I_t = 20$ nA]. (g) $\vartheta = 15^\circ$ [$V_b = 0.005$ V, $I_t = 5$ nA]. The insets of (d,f,g) are Fourier transforms of the corresponding graphene moirés.

The distribution of the ϑ values is confirmed by the variety of moiré superstructures observed by STM at the nanometer scale. Generally, graphene moiré originates from lattice mismatch and/or angular misorientation in two isosymmetric overlapping periodic lattices; herein the situation is further complicated by the symmetry mismatch of the two interface lattices. In figures 2(a-c), from left to right, we show three STM images with increasing misorientation angles: the morphology of graphene moirés changes from parallel stripes to a rhombic network when increasing ϑ from 0° to 15° (figure S8), similarly to graphene on Cu(100)[30]. The atomic structure of these moirés is revealed in the lower panel of figure 2. Figure 2(d) shows a typical striped moiré pattern with $\vartheta = 0^\circ$, where the Fourier transform (inset) confirms the alignment between moiré stripes and one graphene lattice vector. Figures 2(e,f) present zoom-ins on the squares in figure 2(b). By increasing the misorientation angle, the rhombic network modulation in moiré patterns becomes more visible, as evident in figure 2(e), where two graphene rotational domains with $\vartheta = 9.5^\circ$ (lower) and 12.5° (upper) coalesce seamlessly at the locally linear boundary (blue dashed line in figure 2(b)). In fact, it should be noted that, in spite of the apparent different morphology, the moiré patterns for $\vartheta = 9.5^\circ$ and 12.5° (figures 2(e,f)) are both intermediate situations between a strictly striped structure ($\vartheta = 0^\circ$) and an equilaterally rhombic structure ($\vartheta = 15^\circ$). A clear network superstructure can be seen in figures 2(c,g), for $\vartheta = 15^\circ$. Both topographic images (figures 2(c,g)) and the corresponding FT (inset of figure 2(g), from the flat region in figure 2(c)) reveal the moiré supercell with a shape of equilateral rhombus, as expected from the symmetry factors (see the atomic model in figure S7).

Another point worth mentioning is that, through an analysis of more than 50 high-quality, atomic-resolved STM images on different domains (larger than $10 \times 10 \text{ nm}^2$), we found that on both polycrystalline and single crystal samples the misorientation angle ϑ does not assume every possible value in the $0^\circ - 15^\circ$ range but only a set of discrete values. A thorough discussion of these results goes beyond the scope of the present paper and will be

presented elsewhere. The growth conditions appear to affect the relative weight of differently oriented domains, but domains at 0° typically prevail, due to effects possibly related to growth dynamics[47], strain release in graphene[23] or lowering of system energy for particular registries[33]. Complementary information at the mesoscale was obtained by Low Energy Electron Microscopy (LEEM) and related microspot-LEED (μ -LEED), confirming this picture (see figure S10). The LEEM experiments provide also information on the stability of the observed graphene domains, indicating that striped graphene with $\vartheta = 0^\circ$ is more stable than network graphene, as, during sample annealing, the former remains on the surface up to $\sim 650^\circ\text{C}$, while the latter disappears at $\sim 620^\circ\text{C}$.

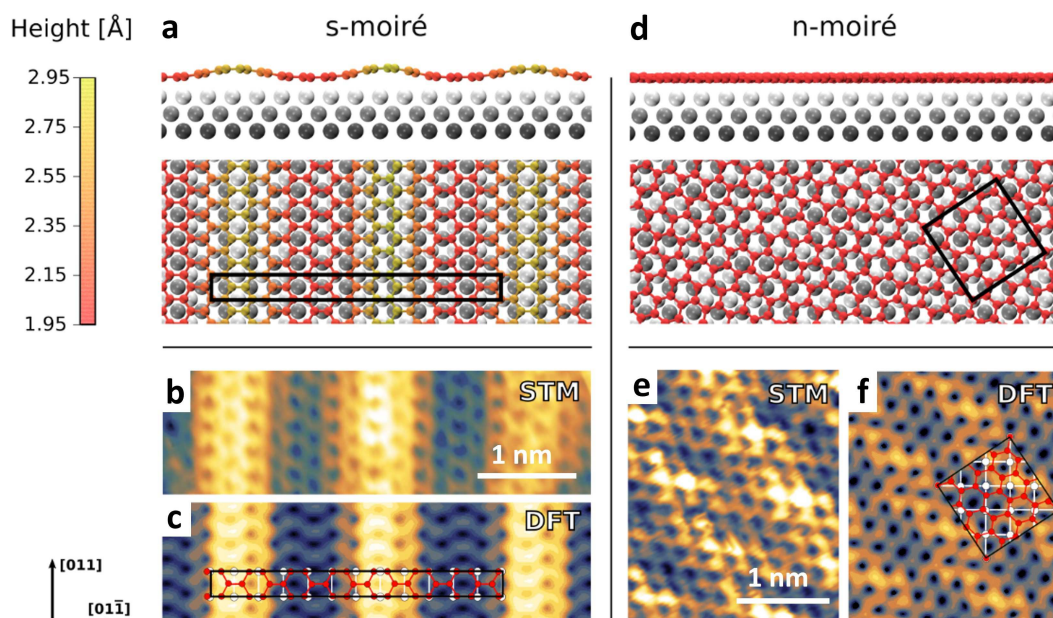
3.2 DFT simulation of *s*- and *n*-moirés

Figure 3. DFT simulations of graphene moirés on Ni(100) with misorientation angles (θ) of 0° (a-c) and 11.3° (d-f). (a,d) Side (upper) and top (lower) views of stick-and-ball models (graphene and Ni(100)) with misorientation angles of 0° (a) and 11.3° (d), respectively. The supercells for DFT simulation are highlighted in the top views. The color bar denotes the height of carbon atoms relative to the outermost layer of nickel atoms. (b,c,e,f) Experimental (b,e) and simulated (c,f) STM images for 0° and 11.3° moiré superstructures. White lines on experimental images are scale bars 5 Å long. Atomic models for moiré supercells are superimposed on the simulated STM images. Scanning parameters: (b) [$V_b = -0.01$ V, $I_t = 3$ nA], (e) [$V_b = -0.2$ V, $I_t = 1$ nA]. Computational parameters: Integrated Local Density of States (ILDOS) iso-surface lying ~ 2 Å above graphene with iso-values of 9×10^{-6} |e|/a₀³ (c) and 1×10^{-4} |e|/a₀³ (f), respectively.

To obtain further insight into the morphological and electronic structures at the graphene-metal interface, ab-initio DFT calculations were performed for moiré patterns with θ of 0° and 11.3° , chosen as prototypical examples of striped and network structures and hereafter named as s-moiré and n-moiré, respectively. For each orientation, the selected simulation cell gives a reasonable description of the real periodicity with a moderate computational effort, as shown in figure 3 (see also Methods and SI for simulation details).

In the case of s-moiré, the absence of superlattice modulation along the moiré stripes (figure 2(d)) indicates that the zigzag periodicity of graphene is commensurate with the unit cell of Ni(100) (figure S11). The modulation is instead evident along the armchair direction of graphene, where repeated registry is realized over several Ni unit cells. A reasonable description can be obtained with 7 graphene periods along its armchair direction matching 12 Ni(100) surface unit cells, resulting in a (12×1) supercell (rectangles in the top view of figure 3(a,c)), compatible with the LEED results. As further evidence, a test performed with a reduced cell did not give a good description (see figure S12). DFT predicts a graphene-Ni distance varying from 1.95 Å to 2.95 Å, with a substantial corrugation (1 Å) along the armchair direction of graphene (Ni $[01\bar{1}]$ direction in figure 3). The low and high regions of graphene alternate twice in each supercell. Besides its periodicity, the moiré superstructure is determined also by the relative translational registry between graphene and Ni. The registry giving the lowest total energy is that minimizing on average the misalignment between C and surface Ni atoms (figure S13). The simulated STM image (figure 3(c)) based on the so-optimized model (figure 3(a)) remarkably reproduces the experiment (figure 3(b)).

The case of n-moiré is more complicated, due to the misalignment between the graphene and substrate lattice vectors. At variance with the elongated rectangular supercell for s-moiré (figure 3(a)), the supercell for

any other angle is in general rhombic (figure 3(d)), in accordance with the tendency of moiré motif evolution for increasing θ (from stripes to rhombic networks). The particular case of n-moiré can be simulated by a relatively small square ($\sqrt{13} \times \sqrt{13}R33.7^\circ$) supercell containing 16 surface Ni atoms and 30 carbon atoms, with a misorientation angle of 11.3° (see figures 3(d,f), 4(b) and S14). A small artificial, anisotropic strain was imposed to the graphene lattice to obtain a repeated registry between carbon and nickel atoms within a reasonable distance for DFT calculation, whereas the real moiré unit cell is probably much larger. Although a two-dimensional modulation is clearly visible in both experimental and simulated STM images (figures 3(e,f)), DFT predicts a very small corrugation (0.2 \AA) and a distance from the substrate ranging from 1.95 \AA to 2.15 \AA (figure 3(d)).

Notably, the height of the lowest graphene regions (1.95 \AA) in both s-moiré and n-moiré is comparable with that on Ni(111) and Ru(0001)[10, 14], indicative of strong interfacial coupling. However, for s-moiré, 'ridges' with adsorption height (2.95 \AA , see figure 3(a)) comparable with interlayer distance in graphite (3.34 \AA) suggest physisorption. Periodically modulated physisorbed and chemisorbed regions have also been reported for graphene on strongly interacting 3-fold metal surfaces, e.g. Ru(0001)[13]. The calculated average adsorption energy (E_{ads} , see Methods) is -0.17 eV per carbon atom, similar to what reported for Ni(111)[10]. Although the contributions from the bright and dark regions cannot be separated, considering the highly anisotropic coupling intensity across the s-moiré domain, the adsorption energies of carbon atoms at the ridge/valley regions are expected to considerably deviate from the average value. In n-moiré, instead, the height distribution of carbon atoms is much more uniform (see figure 3(d)), suggesting isotropic chemisorption across the supercell. Here the calculated average adsorption energy of graphene is -0.20 eV per carbon atom, with a magnitude slightly larger than for s-moiré, although this difference is comparable to the DFT numerical accuracy.

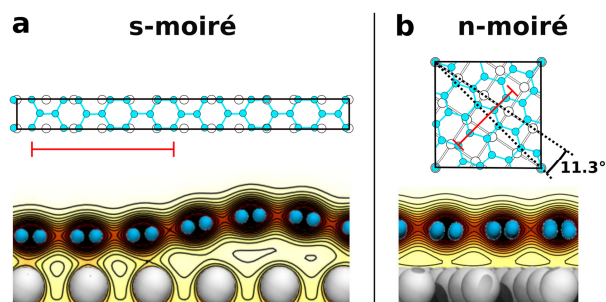


Figure 4. DFT-computed electron distribution at graphene-Ni(100) interface for s-moiré (a) and n-moiré (b).

Upper panels: moiré supercells for DFT simulation, with red lines indicating the orientation and the extension of the cross section for the projection of the electron distribution. The resulting plots are shown in the lower panels. Color scale from light yellow to dark brown indicate electron density going from minimum to maximum values.

The different adsorption configurations for C atoms in s-moiré and n-moiré are corroborated by the electron density plots. Figures 4(a,b) show the cross-section projection along the graphene armchair directions (red lines in the upper panels) for both moirés using the same scale. The interfacial electron distribution between graphene and the outermost nickel layer for the case of s-moiré is characterized by alternate regions of higher and lower electron density (figure 4(a)), indicating that chemisorption only exists when the moiré pattern gets closer to the Ni surface. For n-moiré, instead, the electron density at the interface does not appreciably vary across the moiré cell (figure 4(b)), suggesting a homogeneous interlayer coupling. The different graphene-Ni interactions for s-moiré and n-moiré, confirmed also by the radial distribution function of the carbon-carbon distances (see figure S15), are likely to lead to different electronic structures (figure S16) and possibly chemical

reactivity. In particular, the patterned electron density inhomogeneity for striped moirés could induce periodically modulated electrostatic field or one-dimensional charge accumulation/depletion, which could be exploited for tuning the band structure of graphene, selective modification of its chemical activity, and patterned preparation of one-dimensional nanostructures.

4. Conclusion

Summarizing, monolayer graphene was investigated on both pretreated polycrystalline nickel foils and Ni(100) single crystals. The atomic structure of graphene on the 4-fold (100) substrate was explored by high-resolution STM, revealing a variety of moiré patterns from quasi one-dimensional stripes to two-dimensional rhombic networks, depending on the angular interface misorientation. Two prototypical striped and network moiré superstructures were investigated in details by DFT, revealing distinct interfacial adsorption features. This work rationalizes previous reports of both types of moiré patterns for graphene grown on transition metal (100) facets, indicating the possibility of manipulating the electronic properties of graphene on the nanoscale through the rotational registry of graphene on metallic substrates.

ACKNOWLEDGMENTS

We acknowledge financial support from Italian Ministry of Foreign Affairs, Directorate General for the Country Promotion (Executive Programme with Argentina 2014-2016 (PGR00190)) and from University of Trieste (program “Finanziamento di Ateneo per progetti di ricerca scientifica – FRA 2015”). Z.Z. acknowledges support by the “ICTP TRIL Programme, Trieste, Italy” in the framework of the agreements with the Elettra and CNR-IOM laboratories. Computational resources have been obtained from CINECA through the ISCRA initiative

and the agreement with the University of Trieste. We thank A. Locatelli, O.T. Montes and F. Genuzio for their help during the LEEM/ μ LEED experiments.

REFERENCES

- [1] J. Wintterlin, M.L. Bocquet, Graphene on metal surfaces, *Surf. Sci.* 603 (2009) 1841-1852
- [2] M. Batzill, The surface science of graphene: Metal interfaces, CVD synthesis, nanoribbons, chemical modifications, and defects, *Surf. Sci. Rep.* 67 (2012) 83-115
- [3] P.W. Sutter, J.-I. Flege, E.A. Sutter, Epitaxial graphene on ruthenium, *Nat. Mater.* 7 (2008) 406-411
- [4] X.S. Li, W.W. Cai, J.H. An, S. Kim, J. Nah, D.X. Yang et al, Large-area synthesis of high-quality and uniform graphene films on copper foils, *Science* 324 (2009) 1312-1314
- [5] K.S. Kim, Y. Zhao, H. Jang, S.Y. Lee, J.M. Kim, K.S. Kim et al, Large-scale pattern growth of graphene films for stretchable transparent electrodes, *Nature* 457 (2009) 706-710
- [6] A. Reina, X.T. Jia, J. Ho, D. Nezich, H. Son, V. Bulovic et al, Large area, few-layer graphene films on arbitrary substrates by chemical vapor deposition, *Nano Lett.* 9 (2009) 30-35
- [7] B.Y. Dai, L. Fu, Z.Y. Zou, M. Wang, H.T. Xu, S. Wang et al, Rational design of a binary metal alloy for chemical vapour deposition growth of uniform single-layer graphene, *Nat. Commun.* 2 (2011) 522-527
- [8] Z.Y. Zou, L. Fu, X.J. Song, Y.F. Zhang, Z.F. Liu, Carbide-forming groups IVB-VIB metals: A new territory in the periodic table for CVD growth of graphene, *Nano Lett.* 14 (2014) 3832-3839

- [9] Y.F. Zhang, T. Gao, S.B. Xie, B.Y. Dai, L. Fu, Y.B. Gao et al, Different growth behaviors of ambient pressure chemical vapor deposition graphene on Ni(111) and Ni films: A scanning tunneling microscopy study, *Nano Res.* 5 (2012) 402-411
- [10] F. Bianchini, L.L. Patera, M. Peressi, C. Africh, G. Comelli, Atomic scale identification of coexisting graphene structures on Ni(111), *J. Phys. Chem. Lett.* 5 (2014) 467-473
- [11] L.L. Patera, F. Bianchini, G. Troiano, C. Dri, C. Cepek, M. Peressi et al, Temperature-driven changes of the graphene edge structure on Ni(111): substrate vs hydrogen passivation, *Nano Lett.* 15 (2015) 56-62
- [12] D. Eom, D. Prezzi, K.T. Rim, H. Zhou, M. Lefenfeld, S. Xiao et al, Structure and electronic properties of graphene nanoislands on Co(0001), *Nano Lett.* 9 (2009) 2844-2848
- [13] S. Marchini, S. Günther, J. Wintterlin, Scanning tunneling microscopy of graphene on Ru(0001), *Phys. Rev. B* 76 (2007) 075429
- [14] W. Moritz, B. Wang, M.L. Bocquet, T. Brugger, T. Greber, J. Wintterlin et al, Structure determination of the coincidence phase of graphene on Ru(0001), *Phys. Rev. Lett.* 104 (2010) 136102
- [15] B. Wang, M. Caffio, C. Bromley, H. Früchtl, R. Schaub, Coupling epitaxy, chemical bonding, and work function at the local scale in transition metal-supported graphene, *ACS Nano* 4 (2010) 5773-5782
- [16] E.N. Voloshina, Y.S. Dedkov, S. Torbrügge, A. Thissen, M. Fonin, Graphene on Rh(111): scanning tunneling and atomic force microscopies studies, *Appl. Phys. Lett.* 100 (2012) 241606

- [17] E. Miniussi, M. Pozzo, A. Baraldi, E. Vesselli, R.R. Zhan, G. Comelli et al, Thermal stability of corrugated epitaxial graphene grown on Re(0001), *Phys. Rev. Lett.* 106 (2011) 216101
- [18] C. Tonnoir, A. Kimouche, J. Coraux, L. Magaud, B. Delsol, B. Gilles et al, Induced superconductivity in graphene grown on rhenium, *Phys. Rev. Lett.* 111 (2013) 246805
- [19] Z. Sun, S.K. Hämäläinen, J. Sainio, J. Lahtinen, D. Vanmaekelbergh, P. Liljeroth, Topographic and electronic contrast of the graphene moiré on Ir(111) probed by scanning tunneling microscopy and noncontact atomic force microscopy, *Phys. Rev. B* 83 (2011) 081415
- [20] A.B. Preobrajenski, M.L. Ng, A.S. Vinogradov, N. Martensson, Controlling graphene corrugation on lattice-mismatched substrates, *Phys. Rev. B* 78 (2008) 073401
- [21] L. Gao, J.R. Guest, N.P. Guisinger, Epitaxial graphene on Cu(111), *Nano Lett.* 10 (2010) 3512-3516
- [22] L. Meng, R.T. Wu, L.Z. Zhang, L.F. Li, S.X. Du, Y.L. Wang et al, Multi-oriented moiré superstructures of graphene on Ir(111): experimental observations and theoretical models, *J. Phys.: Condens. Matter* 24 (2012) 314214
- [23] P. Merino, M. Švec, A.L. Pinardi, G. Otero, J.A. Martín-Gago, Strain-driven moiré superstructures of epitaxial graphene on transition metal surfaces, *ACS Nano* 5 (2011) 5627-5634
- [24] A. Dahal, M. Batzill, Graphene-nickel interfaces: a review, *Nanoscale* 6 (2014) 2548-2562
- [25] C. Enderlein, Y.S. Kim, A. Bostwick, E. Rotenberg, K. Horn, The formation of an energy gap in graphene on ruthenium by controlling the interface, *New J. Phys.* 12 (2010) 033014

- [26] I. Pletikosić, M. Kralj, P. Pervan, R. Brako, J. Coraux, A.T. N'Diaye et al, Dirac cones and minigaps for graphene on Ir(111), *Phys. Rev. Lett.* 102 (2009) 056808
- [27] H.I. Rasool, E.B. Song, M.J. Allen, J.K. Wassei, R.B. Kaner, K.L. Wang et al, Continuity of graphene on polycrystalline copper, *Nano Lett.* 11 (2011) 251-256
- [28] Y. Zhang, L. Gomez, F.N. Ishikawa, A. Madaria, K. Ryu, C. Wang et al, Comparison of graphene growth on single-crystalline and polycrystalline Ni by chemical vapor deposition, *J. Phys. Chem. Lett.* 1 (2010) 3101-3107
- [29] R.S. Weatherup, B.C. Bayer, R. Blume, C. Ducati, C. Baetz, R. Schlögl et al, In situ characterization of alloy catalysts for low-temperature graphene growth, *Nano Lett.* 11 (2011) 4154-4160
- [30] J.-W. Cho, L. Gao, J.F. Tian, H.L. Cao, W. Wu, Q.K. Yu et al, Atomic-scale investigation of graphene grown on Cu foil and the effects of thermal annealing, *ACS Nano* 5 (2011) 3607-3613
- [31] A. Locatelli, C. Wang, C. Africh, N. Stojić, T.O. Mentesh, G. Comelli et al, Temperature-driven reversible rippling and bonding of a graphene superlattice, *ACS Nano* 7 (2013) 6955-6963
- [32] N.A. Vinogradov, A.A. Zakharov, V. Kocovski, J. Ruzs, K.A. Simonov, O. Eriksson et al, Formation and structure of graphene waves on Fe(110), *Phys. Rev. Lett.* 109 (2012) 026101
- [33] D. Usachov, A.M. Dobrotvorskii, A. Varykhalov, O. Rader, W. Gudat, A.M. Shikin et al, Experimental and theoretical study of the morphology of commensurate and incommensurate graphene layers on Ni single-crystal surfaces, *Phys. Rev. B* 78 (2008) 085403

- [34] Y. Murata, V. Petrova, B.B. Kappes, A. Ebnonnasir, I. Petrov, Y.-H. Xie et al, Moiré superstructures of graphene on faceted nickel islands, *ACS Nano* 4 (2010) 6509-6514
- [35] A. Politano, Quasi-freestanding graphene on Ni(110): A graphene/metal contact with suppressed interface states, *Nano Res.* 9 (2016) 1795-1800
- [36] D.A. Pudikov, E.V. Zhizhin, A.G. Rybkin, A.A. Rybkina, Y.M. Zhukov, O.Y. Vilkov et al, Electronic structure of graphene on Ni surfaces with different orientation, *Mater. Chem. Phys.* 179 (2016) 189-193
- [37] L. Hyonik, L. Seulah, H. Juree, L. Sang Geun, L. Jae-Hong, L. Taeyoon, Graphene converted from the photoresist material on polycrystalline nickel substrate, *Jpn. J. Appl. Phys.* 51 (2012) 06FD17
- [38] Q.K. Yu, J. Lian, S. Siriponglert, H. Li, Y.P. Chen, S.-S. Pei, Graphene segregated on Ni surfaces and transferred to insulators, *Appl. Phys. Lett.* 93 (2008) 113103
- [39] D. Necas, P. Klapetek, Gwyddion: an open-source software for SPM data analysis, *Cent. Eur. J. Phys.* 10 (2012) 181–188
- [40] G. Paolo, B. Stefano, B. Nicola, C. Matteo, C. Roberto, C. Carlo et al, QUANTUM ESPRESSO: a modular and open-source software project for quantum simulations of materials, *J. Phys.: Condens. Matter* 21 (2009) 395502
- [41] J.P. Perdew, K. Burke, M. Ernzerhof, Generalized gradient approximation made simple, *Phys. Rev. Lett.* 77 (1996) 3865-3868

- [42] S. Grimme, Density functional theory with London dispersion corrections, Wiley Interdiscip. Rev.: Comput. Mol. Sci. 1 (2011) 211-228
- [43] H.J. Monkhorst, J.D. Pack, Special points for Brillouin-zone integrations, Phys. Rev. B 13 (1976) 5188-5192
- [44] M. Methfessel, A.T. Paxton, High-precision sampling for Brillouin-zone integration in metals, Phys. Rev. B 40 (1989) 3616-3621
- [45] W. Humphrey, A. Dalke, K. Schulten, VMD: Visual molecular dynamics, Journal of Molecular Graphics 14 (1996) 33-38
- [46] J. Tersoff, D.R. Hamann, Theory of the scanning tunneling microscope, Phys. Rev. B 31 (1985) 805-813
- [47] L.L. Patera, C. Africh, R.S. Weatherup, R. Blume, S. Bhardwaj, C. Castellarin-Cudia et al, In situ observations of the atomistic mechanisms of Ni catalyzed low temperature graphene growth, ACS Nano 7 (2013) 7901-7912